

***Final Draft***  
**of the original manuscript:**

Scheider, I.; Xiao, T.; Huber, N.; Mosler, J.:

**On the interaction between different size effects in fibre reinforced PMMA: Towards composites with optimised fracture behaviour**

In: Computational Materials Science (2013) Elsevier

DOI: [10.1016/j.commatsci.2013.04.027](https://doi.org/10.1016/j.commatsci.2013.04.027)

# On the interaction between different size effects in fibre reinforced PMMA: towards composites with optimised fracture behaviour

I. Scheider<sup>1\*</sup>, T. Xiao<sup>1</sup>, N. Huber<sup>1</sup>, J. Mosler<sup>1,2</sup>

<sup>1</sup>*Helmholtz-Zentrum Geesthacht, Institute of Materials Research, Materials Mechanics, Geesthacht, Germany*

<sup>2</sup>*TU Dortmund, Institute of Mechanics, Dortmund, Germany.*

\*corr. author: ingo.scheider@hzg.de

---

## Abstract

This paper is concerned with a numerical investigation of different size effects and their interactions in fibre reinforced PMMA. Focus is on the mechanical response – particularly on the damage and the fracture behaviour. The performed numerical studies are based on finite element simulations in which representative volume elements with different microstructures have been virtually mechanically tested and compared to each other. The underlying numerical model captures the most relevant mechanical mechanisms such as damage evolution, crack propagation and failure by a cohesive zone model. Previous studies have shown that the effective macroscopic fracture properties can be changed by varying the thickness of the fibres. In this paper, an additional size effect resulting from a variation of the fibres' lengths and the interaction between both size effects is carefully analysed. By understanding such size effects, the observed failure mechanisms can be changed effectively and the properties of the considered composite can be improved significantly. For instance, it will be shown that a composite can be designed which shows a high strength as well as a high fracture energy.

Keywords: Composites; Size effect; short fibre; cohesive zone model; debonding, bio-inspired material

---

## 1. Introduction

Biological materials often show a hierarchical microstructure which, compared to conventional solids, leads to superior properties. According to [1-3], such properties encompass an increased stiffness, an increased strength and a better damage tolerance. In a nutshell, the improved properties of biological materials with a hierarchical microstructure are often due to size effects. One representative example is the size-dependence of the fracture strength. As shown for instance by Gao et al. (see [4, 5]), the fracture strength of fibres with very small diameters (typically in the range of a few nanometres) can reach the theoretical strength of the underlying material. Indeed, a high fracture strength at the nano- or micro-scale does not imply a high fracture strength at the macroscale. In biological materials, the superior properties at the lowest scale are conserved at the macroscale through a hierarchical microstructure (see [4, 5]). Due to the impressive mechanical properties of biological materials, the development of bio-inspired, new man-made materials by copying the aforementioned hierarchical microstructure has become an active research area. A large initiative in Japan started as early as in 1994, cf. [6].

Since the underlying mechanisms eventually resulting in superior properties of biological materials with a hierarchical microstructure are usually very complex, constitutive models are required in order to understand such materials – also from a quantitative point of view. Such models can be found, e.g., in [5, 7]. In particular, the interaction between material parameters and geometrical dimensions and its effect on failure properties of the material has been investigated by Gao et al., see [4, 5]. Within the cited papers, the authors employed a relatively simple material model, together with a practical homogenisation approach. Qualitatively, the authors

could reproduce the fracture response observed in biological materials with a hierarchical microstructure over several hierarchical levels.

The approximations made by Gao et al. (e.g., one-dimensional model, no debonding of the fibres, type of the pre-existing cracks, etc.) were partly justified in [8] through finite element simulations. In line with [4, 5], it was shown in [8] that a single fibre reaches its theoretical strength, if its diameter is smaller than a certain threshold (the respective representative volume element considered in [8] is shown in Figure 1). However, this threshold indeed strongly depends on the shape and orientation of the pre-existing micro-cracks. A centre crack, as assumed in the one-dimensional model used in [4, 5], usually leads to an overestimation of the flaw tolerance. Furthermore, and in contrast to the results reported in [4, 5], the more realistic finite element simulations performed in [8] predicted that the fracture energy of the composite might not decrease with size, but can also increase due to a changing failure mechanism.

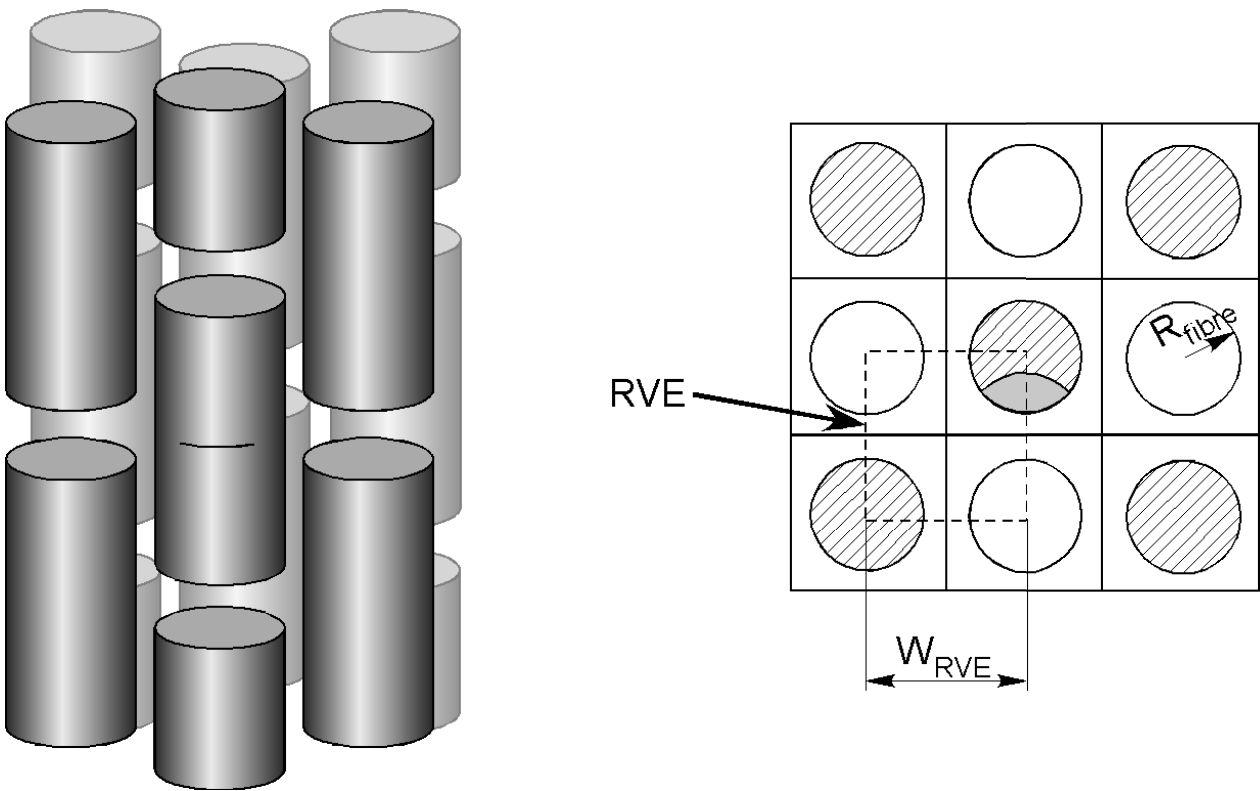


Figure 1: Microstructure investigated in [8]: Composite reinforced by short unidirectional fibres

The present investigation extends the findings reported in [8] with respect to two different aspects:

The first new aspect is the practical relevance of the model: Whereas the paper [8] addressed flaw tolerance of fibre reinforced composites for an artificial material, the present paper is concerned with the optimisation of the structural performance of a real material. To be more precise, PMMA strengthened by ceramic ( $\text{TiO}_2$ ) fibres is considered. Hierarchical bio-inspired materials made from these ingredients have already been experimentally tested in [9]. Particle sizes and shapes of the inclusions can be triggered exactly according to their needs, and any number of hierarchy levels can be produced.

In order to further understand the processing techniques proposed in [9], a mechanically sound constitutive model representing the microstructural characteristics is required. To provide such a model and eventually optimise the composite material is one of the goals pursued in the present paper.

The second extension – and probably the key contribution of the present paper – is the investigation of the interactions between different size effects. In addition to the size effect caused by the thickness of the fibres, the size effect related to the lengths of the fibres is now also considered. For this reason, the set of failure modes captured by the finite element model has to be enriched. It will be shown that, by combining and tuning the aforementioned size effects, a composite can be designed showing improved mechanical properties such as a high strength and, simultaneously, a high fracture energy.

## **2. Micromechanical Modelling of fibre-reinforced PMMA**

In order to capture the most relevant mechanical features, in particular the failure behaviour and hence the damage mechanism, the fibre-reinforced PMMA is modelled by means of a micromechanical description. For that purpose, the underlying microstructure is represented by a suitable representative volume element (RVE). The interested reader is referred to [10] and references cited therein for further details.

It is well known that the simulation of an RVE is independent of its absolute size as long as no localization of strains occurs. However, in the case of material softening due to damage and crack propagation as considered here, the RVE is size dependent, see e.g. [11, 12], hence, special attention needs to be paid regarding the size of the RVE.

### *2.1. Bulk material*

Pure PMMA has been tested in [13] by micro indentation using a flat punch indenter. Within the vast majority of nonlinear PMMA simulations, the polymer is represented by means of a standard J2-plasticity model with isotropic hardening. This assumption is also made in the present paper. The model parameters have been calibrated by a standard least-squares-fit in which the experimental force-indentation depth data as reported in [13] were compared to the model predictions. The respective measurements and the predictions obtained with the optimised material parameters are shown in Figure 2 (left picture).

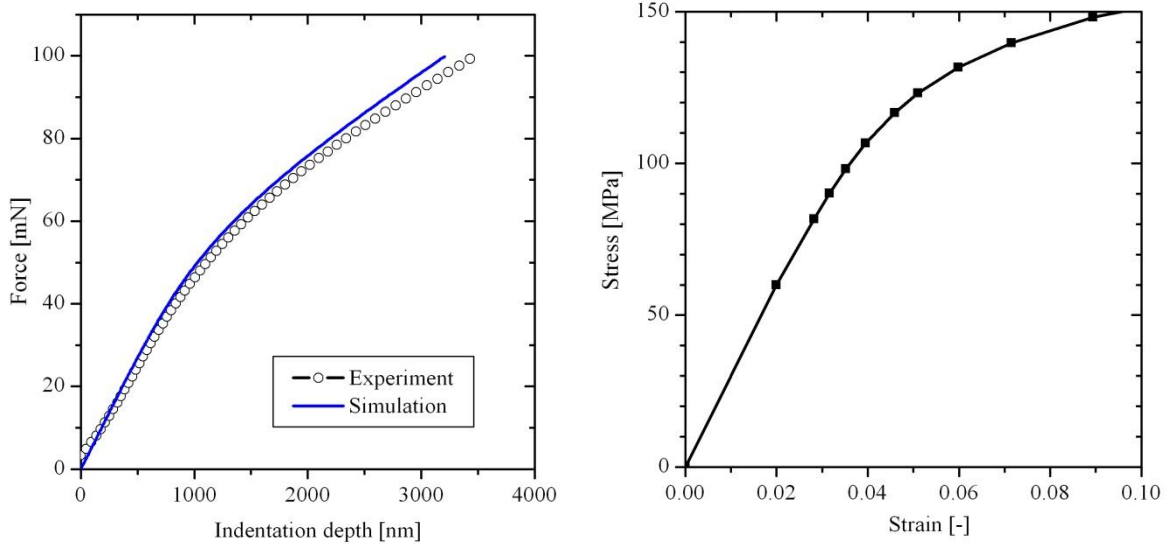


Figure 2: Mechanical response of PMMA. Left: Micro-indentation experiment vs. simulation Right: stress-strain-relation used in the simulation

The underlying stress-strain curve for the PMMA is also displayed in Figure 2 (right picture), while the respective model parameters are summarised in Table 1. The identified model parameters agree reasonably well with those reported in the literature, cf. [14]. It is emphasised that the employed time-independent plasticity model cannot capture some of the effects important for PMMA such as the creep behaviour, see e.g. [15]. However, such effects are not the focus of the present study and, therefore, a rate-independent model represents a reasonable choice.

For the ceramic oxide fibres,  $\text{TiO}_2$  (Rutile), the material model and its parameters are taken from the literature. Before cracking, a standard isotropic hyperelastic constitutive model is employed. In line with the range of the Young's modulus  $E$  documented in the literature (230 GPa in [33] up to 330 GPa in [34]) and the Poisson's ratio  $\nu$ , the elasticity constants are set to  $E=270$  GPa and  $\nu = 0.27$ .

Table 1: Model parameters for the bulk materials: For both materials, elasticity is modelled by standard isotropic Hooke type models. In the case of PMMA, inelastic effects are taken into account by standard rate-independent plasticity theory with a yield stress of 60 MPa.

|                         | $E$<br>[GPa] | $\nu$<br>[-] | Yield strength<br>[MPa] |
|-------------------------|--------------|--------------|-------------------------|
| Polymer, PMMA           | 3            | 0.4          | 60                      |
| Ceramic, $\text{TiO}_2$ | 270          | 0.27         | -                       |

## 2.2. Material interfaces

In addition to the bulk material, the mechanical response at the material's interfaces is of utmost importance. A natural framework in order to capture mechanical effects at material interfaces is provided by a so-called *cohesive zone model*. This phenomenological model has the

advantage that it can be used on the micro- as well as on the macroscale. Concerning applications of this model to the microscale, debonding of reinforced materials was started to be modeled in the early 1990s [16] and has been put forward by many groups, see e.g. [10, 17-19] for fibre reinforced composites, and also for micromechanical modeling of intergranular fracture of polycrystalline materials, e.g. [20-22].

In contrast to a classical stress-strain-type relationship, cohesive zone models are based on traction-separation-relations, e.g., crack opening vs. stresses across a not fully opened crack. Such a relation can be written in the general form

$$\mathbf{T}_s = \mathbf{T}_s(\llbracket \mathbf{u} \rrbracket) \quad (1)$$

where  $\mathbf{T}_s$  is the traction vector and  $\llbracket \mathbf{u} \rrbracket$  is the displacement jump or displacement discontinuity. Without going too much into detail, a cohesive zone model based on damage mechanics is applied. It relies on a physically sound mixed-mode traction-separation-relation of the type

$$\mathbf{T}_s = (1 - d) c \llbracket \mathbf{u} \rrbracket \quad (2)$$

In Eq. (1),  $c$  is the interface's stiffness and  $d \in [0; 1]$  is a scalar-valued damage parameter. While the virgin material is characterised by  $d = 0$ , a fully open stress-free crack is signalled by  $d = 1$ . Damage initiation is checked by a stress-like criterion. It is assumed that microcracks or damage nucleate if the maximum tensile stress reaches  $T_0$ . Upon further loading, the damage parameter increases monotonically. In the numerical studies discussed in the present paper, the evolution of  $d$  is chosen, such that the resulting traction-separation-law is bilinear, see [8]. A fully open macroscopic crack is assumed if the critical separation (crack width) reaches  $\delta_0$ . The respective work of separation corresponds to a fracture energy of  $\Gamma_0$ . For further details on cohesive zone models, the interested reader is referred to [23].

The cohesive model properties of PMMA are taken from the literature; cf. [14] and [24, 25]. For ceramics, the number of papers dealing with fracture properties is naturally large. The authors chose the material parameters in line with references [26] and [27]. In this connection, the fracture energy was derived from the fracture toughness.

While characteristic material parameters can be found in the literature for PMMA as well as for ceramic fibres, that is not the case for the interface between the ceramic fibres and the polymer. The properties of this interface depend on various factors, mostly influenced by the production of the underlying constituents and the processes during the composition. Therefore, reasonable assumptions are necessary. In the computations, the interface strength is taken as  $T_0 = 40$  MPa, and the fracture energy as  $40$  J/m<sup>2</sup>. However, in order to check the sensitivity of the results, the parameters have also been varied. A summary of the parameters required for the cohesive zone model is given in Table 2.

Table 2: Model parameters for the cohesive zone model capturing the mechanical response of different material interfaces

|                                 | Fracture<br>strength | Fracture<br>energy                | Critical<br>separation          |
|---------------------------------|----------------------|-----------------------------------|---------------------------------|
|                                 | $T_0$<br>[MPa]       | $\Gamma_0$<br>[J/m <sup>2</sup> ] | $\delta_0$<br>[ $\mu\text{m}$ ] |
| Polymer, PMMA                   | 80                   | 460                               | 11.5                            |
| Ceramic, TiO <sub>2</sub>       | 300                  | 38                                | 0.25                            |
| Interface PMMA-TiO <sub>2</sub> | 40                   | 40                                | 2                               |

### 3. Size effect studies

#### 3.1. Numerical model

In order to study the size effect in fibre reinforced PMMA, a representative volume element consisting of four quarter fibres embedded in matrix material is considered (see Figure 3a). A similar RVE was also employed in [8, 28]. It bears emphasis that the scaling relationship of bulk energies (standard stress-strain-based models) and that of interface energies (cohesive zone models) naturally introduced a length scale, as already demonstrated in [8, 28]. Within the cited references, it was shown that the diameter of the fibres influences the observed failure mechanisms, and thus, the resulting strength and fracture energy. The present study differs from the one reported in [8, 28] for three reasons. Firstly the bulk model is now nonlinear and also covers dissipation (rate-independent plasticity theory). Secondly two interacting size effects will be considered: the length of the fibres as well as their diameter. Thirdly more realistic failure modes are included in the underlying finite element models.

Regarding the interaction between the aforementioned failure modes, the aspect ratio (length-to-width ratio of the RVE) is varied between  $a_{\text{RVE}} := L_{\text{RVE}}/W_{\text{RVE}} = 1$  and  $a_{\text{RVE}} = 4.5$ , while the volume fraction of the fibre content is fixed to 57%, and the fibre radius is always 45% of the width of the RVE. With these assumptions, the aspect ratio of the fibre results in  $a_{\text{fibre}} = L_{\text{fibre}}/R_{\text{fibre}} = [1.9 - 8.67]$ , see Figure 3b). The size of the surface crack in the precracked fibre,  $A_{\text{crack}}$ , has been fixed to 20% of the fibre area,  $A_{\text{crack}} = 0.2A_{\text{fibre}} = 0.2 \frac{\pi R_{\text{fibre}}^2}{4}$ .

In order to account for more realistic failure modes, and in contrast to the model utilized in [8, 28], additional planes where material failure can occur (cracks or debonding) have been inserted into the finite element simulation. In particular, the matrix can now not only crack in the symmetry plane, but also in the plane where the upper fibre ends, Figure 3c). Certainly, cohesive zone models could be inserted everywhere in the finite element discretization in principal. However, that would lead to a numerically inefficient model. For this reason, and as a compromise between physics resolution and numerical efficiency, material separation is assumed to occur only in the planes highlighted in Figure 3c).

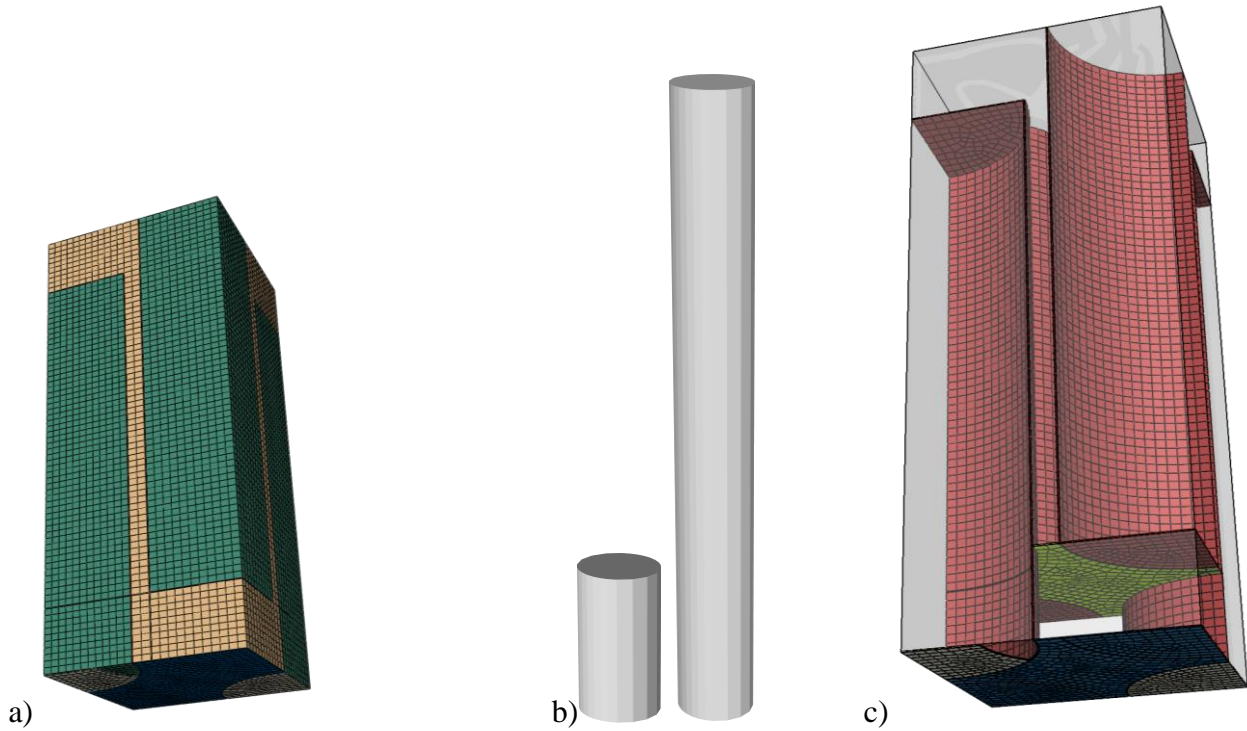


Figure 3: FE model of the representative volume element: a) Whole model containing a polymer matrix (light) and ceramic fibres (dark), shown for an aspect ratio of  $a_{\text{RVE}} = 3$ ; b) Fibre variation between  $a_{\text{fibre}} = 1.9$  and  $a_{\text{fibre}} = 8.7$ ; c) cohesive interfaces included in the model for possible crack extension and debonding

The different representative volume elements are virtually tested. Uniaxial straining is considered, i.e., the side faces are fixed in their normal directions, the symmetry plane in which the crack is located is also fixed, and the upper surface is loaded by a uniform displacement. In line with the previously reported numerical analyses [8, 28], an imperfection in the form of a pre-existing crack within one of the fibres has been modeled.

### 3.2. Results

Within the finite element analyses, four different failure mechanisms can be observed. They depend on the aspect ratio and the fibres' diameter. The respective failure mechanisms are shown in Figure 4. They can be characterised by the degree of debonding between the fibres and the surrounding PMMA matrix. Accordingly, they are referred to in the following as (pure) debonding (a), partial debonding (b), small debonding (c) and breaking (d). In the debonding case (a), the pre-existing crack does not extend at all, but the fibre debonds from the matrix material. In all other cases, the pre-cracked fibre fails by propagation of the existing flaw and debonding starts from the head of the fibre and then proceeds to the fibre centre.

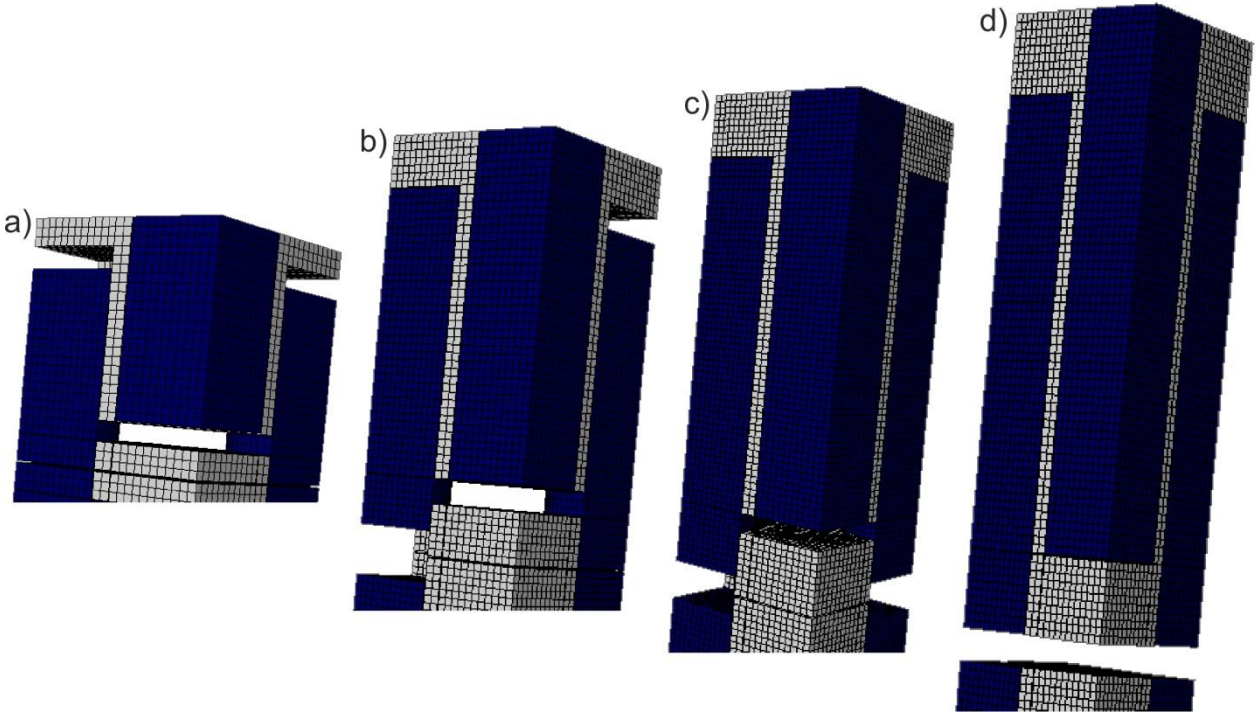


Figure 4: Different failure mechanisms observed in the finite element simulations (from left to right the effect of debonding between the fibres and the surrounding PMMA matrix decreases): debonding (a), partial debonding (b), small debonding (c) and breaking (d).

The type of failure mechanism certainly shows a pronounced effect on the load carrying capacity. In order to compare different RVE sizes, the predicted stress response  $\sigma$  is evaluated (force divided by the cross section area,  $A_{RVE} = W_{RVE}^2 - A_{crack}$ ). The respective  $\sigma$  versus remote displacement  $u$  diagrams for the RVE width  $W_{RVE} = 30 \mu\text{m}$  and for four different aspect ratios are shown in Figure 5. One can see that the stress decreases rapidly after reaching the peak stress, if both fibres at the symmetry plane break (diagrams for  $a_{RVE}=2.2$  and  $a_{RVE}=3.0$ ). This is also the case if only one fibre breaks ( $a_{RVE}=1.8$ ). However, the load drop is smaller. The second loading regime after the stress drop is mostly related to debonding. Except for the RVE with  $a_{RVE}=3.0$ , the interface and/or the fibre fail after the RVE has reached an elongation of  $2 \mu\text{m}$ . For the RVEs with  $a_{RVE}=1.8 - a_{RVE}=2.2$  the polymer eventually fails in the plane of the fibre head. The failure mechanism for the RVE with  $a_{RVE}=3.0$  differs from the previously described ones. This RVE does not fail before a remote displacement of  $11.5 \mu\text{m}$ . The stress carrying capacity in the regime of  $2 \mu\text{m} < u < 11.5 \mu\text{m}$  remote displacement is thus highest for this RVE. From a mechanical point of view, this regime is dominated by damage in the polymer matrix.

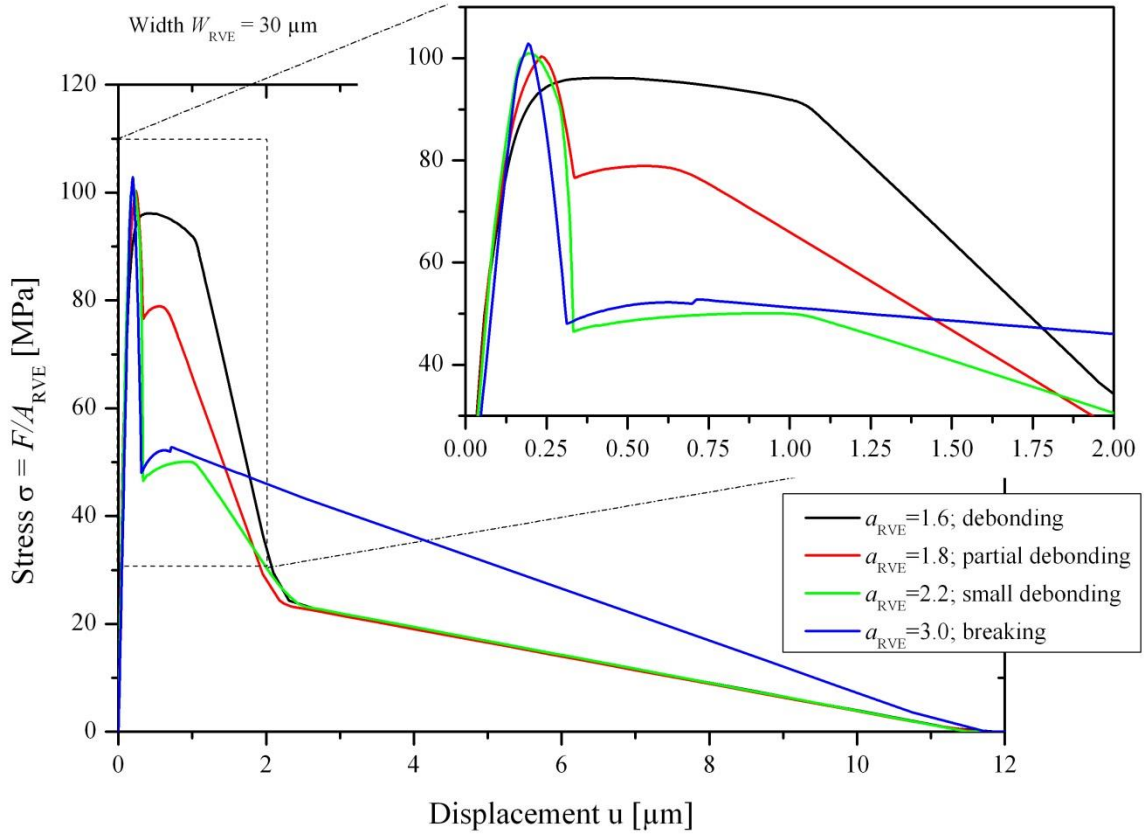


Figure 5: Stress-displacement diagram for RVEs showing different failure mechanisms ( $W_{\text{RVE}} = 30 \mu\text{m}$  and  $a_{\text{RVE}}$  is varied between  $a_{\text{RVE}}=1,6 - a_{\text{RVE}}=3,0$ )

The peak stress  $\sigma_{\text{peak}}$  and the total energy  $G = \int \sigma du$  (the fracture energy) are evaluated for various aspect ratios and widths. The computed results are shown in Figure 6 and in Figure 7. In the same diagrams, the transitions between the four aforementioned failure mechanisms according to Figure 4 are also plotted. According to Figure 6, the highest stress is observed for RVEs with thin long fibres. In this case, the peak stress almost reaches the theoretical strength of 140 MPa, which is calculated as a weighted average between the cohesive strength of ceramic and PMMA, i.e.:

$$\begin{aligned} \sigma_{\text{theor}} &= (T_{0,\text{cer}}(2A_{\text{fibre}} - A_{\text{crack}}) + T_{0,\text{PMMA}}A_{\text{PMMA}})/A_{\text{RVE}} \\ A_{\text{PMMA}} &= A_{\text{RVE}} - (2A_{\text{fibre}} - A_{\text{crack}}) \end{aligned} \quad (3)$$

The respective failure mode is of type “breaking” (type (d) as defined in Figure 4). Above an aspect ratio of approximately 2.5 (i.e. when both fibres break – the *small debonding* and the *breaking* mode) the peak stress is almost invariant with respect to the aspect ratio of the fibres. All fibres showing such a shape are long enough to transfer the stress from the polymer to the fibre until it breaks.

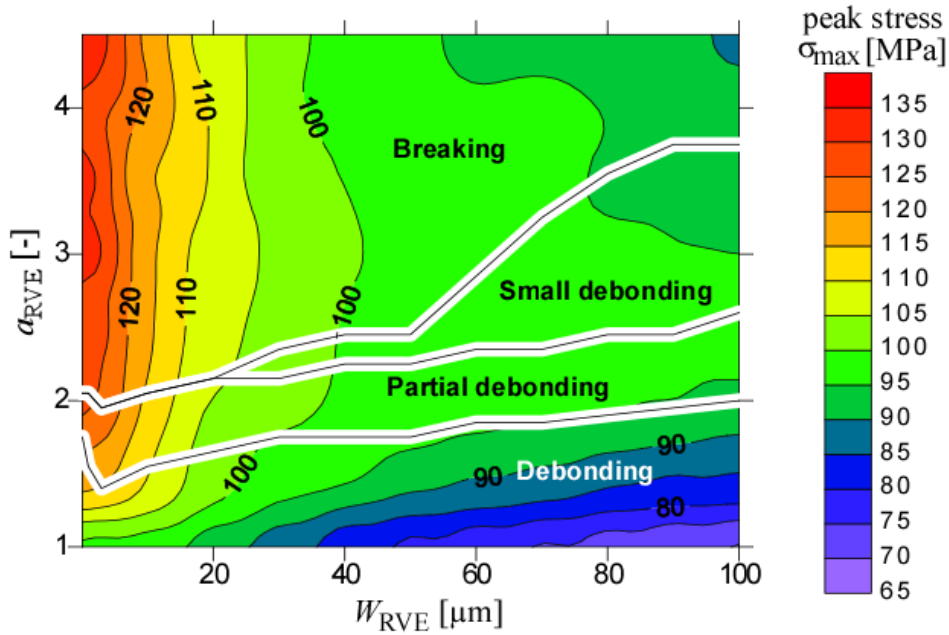


Figure 6: Peak stress (fracture strength) as a function of aspect ratio and width of the RVE. The transition lines between the different failure mechanisms as shown in Figure 4 are also included in the diagram

As evident from Figure 6, the observed failure mechanisms mainly depend on the aspect ratio  $a_{\text{RVE}}$  of the RVE. Only the transition between the failure modes “small debonding” and “breaking” is significantly affected by the width of the RVE. A reason for this width dependence is the crucial importance of the absolute debonding length in this region due to the high critical shear separation of the fibre-matrix interface (2  $\mu\text{m}$ , see Table 2).

Furthermore, Figure 6 shows that the peak stress changes only slightly at the transition lines between the different failure modes. However, while the peak stress mostly depends on the size of the RVE in the case of “breaking”, it mainly depends on the aspect ratio for the failure mode “debonding”.

For conventional materials, a high fracture energy usually contradicts a high fracture strength. That can be seen for the failure mode debonding in Figures 6 and 7, where the highest fracture energy is observed for large fibres whereas the fracture strength shows an opposite trend. However, effects contradicting this general rule (fracture energy vs. fracture strength) are also visible in the figures, e.g., a high fracture energy and a high fracture strength can be seen in the breaking failure mode for small RVEs. Furthermore, the energy strongly depends on the underlying failure mechanism. While a large amount of energy can be dissipated by breaking or debonding, there is a sharp decrease in energy for small debonding or partial debonding.

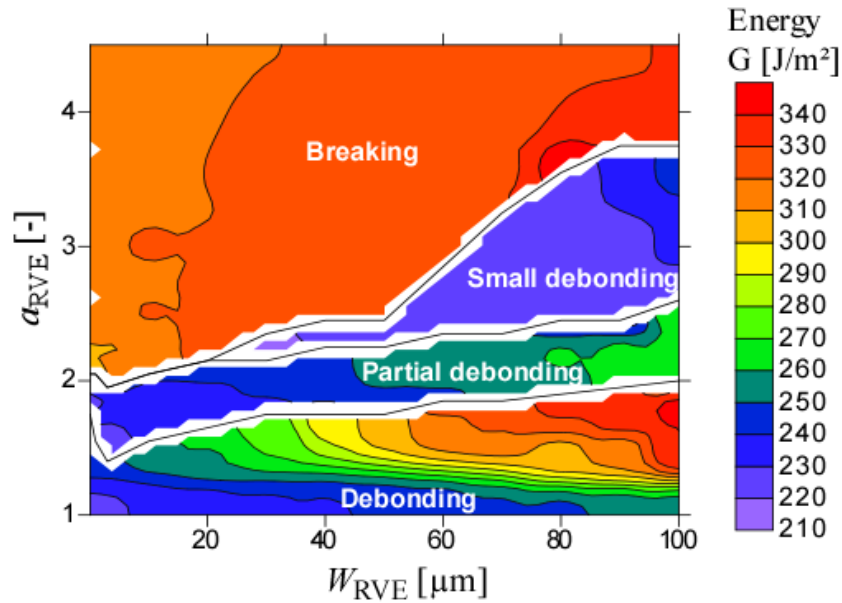


Figure 7: Diagram showing the fracture energy of the RVE for various sizes and aspect ratios. The transition lines between the different failure mechanisms as shown in Figure 4 are also included in the diagram

#### 4. Discussion of the results

##### 4.1. Comparison to previous investigations – Influence of the failure modes

Figure 6 and Figure 7 are very different compared to the respective diagrams reported in the previous publication [28] (see Figure 8). In the case of the fracture strength, the difference between the current study and the one in [28] is mainly related to the logarithmic scaling in Figure 8. By way of contrast, the logarithmic scaling does not explain the discrepancies regarding the fracture energy. For instance, and different to the present study, breaking has a very low energy in [28], while the energy for debonding is high. The reasons for this different response are twofold. The first reason is obvious: A different composite is considered in [28]. To be more precise, the fracture energy of the current PMMA is significantly larger than that of the matrix material in [28], while the fracture energy of the fibre is much lower than before. The second reason, however, is not that obvious. In the present study, additional failure mechanisms have been taken into account. They lead to partial debonding, a failure mode that has not been included in [28]. For this reason, debonding is predicted instead in [28].

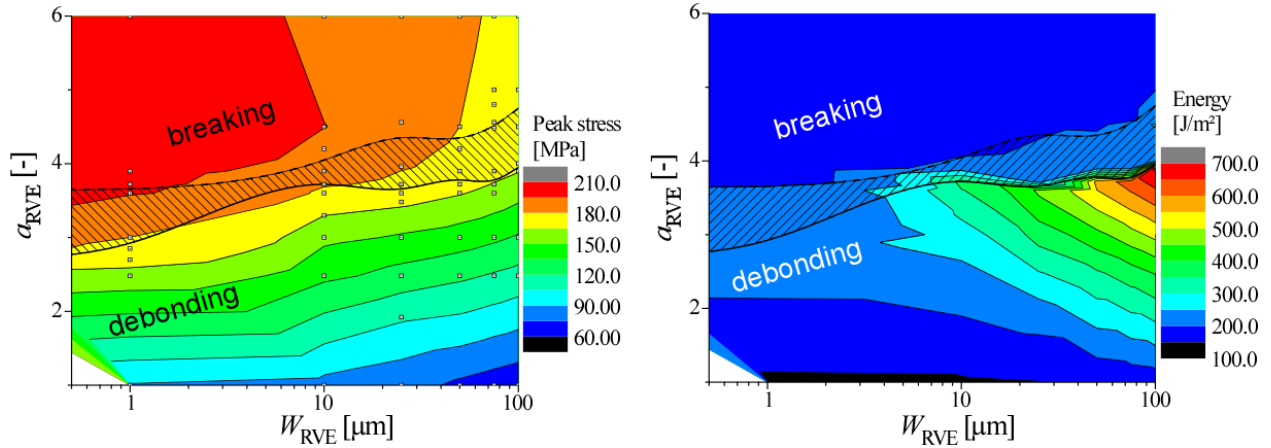


Figure 8: Results for RVE studies reported in [28]. Left: fracture strength; Right: fracture energy.

#### 4.2. Effect of the polymer-ceramic interface – sensitivity analysis of the interface's properties

Only little is known about the bond strength of the ceramic-polymer interface and thus, about the respective parameters of the cohesive zone. However, these parameters do usually have an effect on the RVE's response. For this reason, a sensitivity analysis of the material parameters of the ceramic-polymer interface is carried out here. The parameters that will be varied are the cohesive strength and the cohesive energy (fracture energy).

The results for different cohesive strengths (between  $T_0 = 20$  and  $T_0 = 50$  MPa) and for two different cohesive energies (40 J/m<sup>2</sup> and 100 J/m<sup>2</sup>) are shown in Figure 9 for an RVE with  $W_{\text{RVE}} = 10$  μm. In this diagram, the peak stress is displayed, the respective fracture energies are summarised in Figure 10. In Figure 9 one can see that the cohesive strength has a strong effect on the peak stress. A change in cohesive energy does not change the peak stress significantly for the higher cohesive strength,  $T_0 = 40$  MPa, (compare the green and the blue curve in Figure 9), whereas for  $T_0 = 20$  MPa there is a significant difference as long as the debonding failure mechanism occurs. That is expected, since on the one hand the fracture energy usually mostly influences the softening regime (post peak behavior) and not the peak stress, on the other hand in debonding mode the long crack propagation phase along the fibre leads to higher load carrying capacities and thus higher peak stress. The upper bound for the peak stress is given by a perfectly bonded interface, which is also shown in the figure.

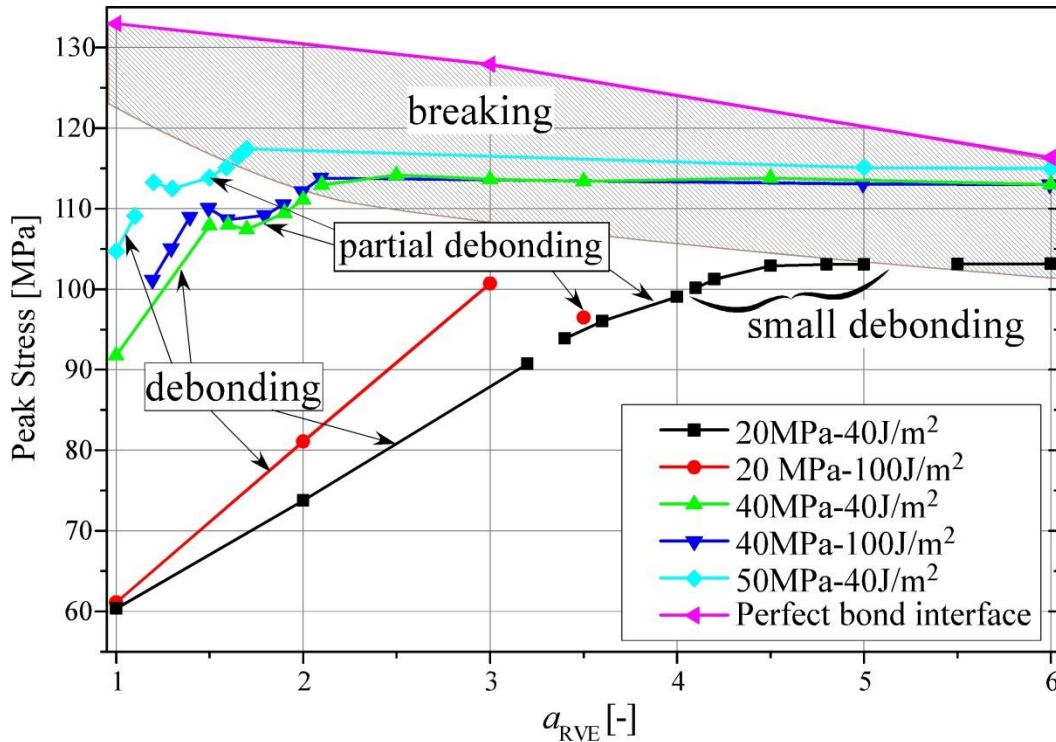


Figure 9: Effect of the ceramic-polymer interfaces on the peak stress and the failure mechanisms for an RVE with  $W = 10 \mu\text{m}$ . Sensitivity of the RVE's fracture strength (peak stress) depending on the cohesive strength and fracture energy of the ceramic-polymer interfaces

Figure 9 also contains the transitions between the different failure mechanisms (disconnected lines show the mechanism change; furthermore, the breaking regime is hatched). As it is evident from this diagram, debonding is more likely to occur if the cohesive strength of the interface is smaller. However, breaking always occurs if the fibre is sufficiently long. Small debonding can only happen if the polymer ceramic interface is much weaker than the polymer (for the RVE with  $W = 10 \mu\text{m}$ ).

The influence of the polymer-ceramic interface on the fracture energy is shown in Figure 10. In this figure, the case "perfect bonding" serves as a reference solution. For a perfect bond, the failure energy does not depend on the aspect ratio if breaking occurs. If debonding is taken into account, the fracture energy depends linearly on the aspect ratio (in a piecewise manner). This is due to the scaling of the RVE's fracture energy: It scales linearly with the absolute length of the fibre in this case. Interestingly, the transition between the different failure mechanisms depends strongly on the cohesive strength, but only slightly on the cohesive energy. For example, the transition from debonding to partial debonding occurs at an aspect ratio of 1.5 for the interface parameters  $T_0 = 40 \text{ MPa}$ ,  $\Gamma_0 = 100 \text{ J/m}^2$  and at an aspect ratio of 1.6 for  $T_0 = 40 \text{ MPa}$ ,  $\Gamma_0 = 40 \text{ J/m}^2$ . In addition, one can see that the perfectly bonded interface is not the best solution with respect to the fracture energy.

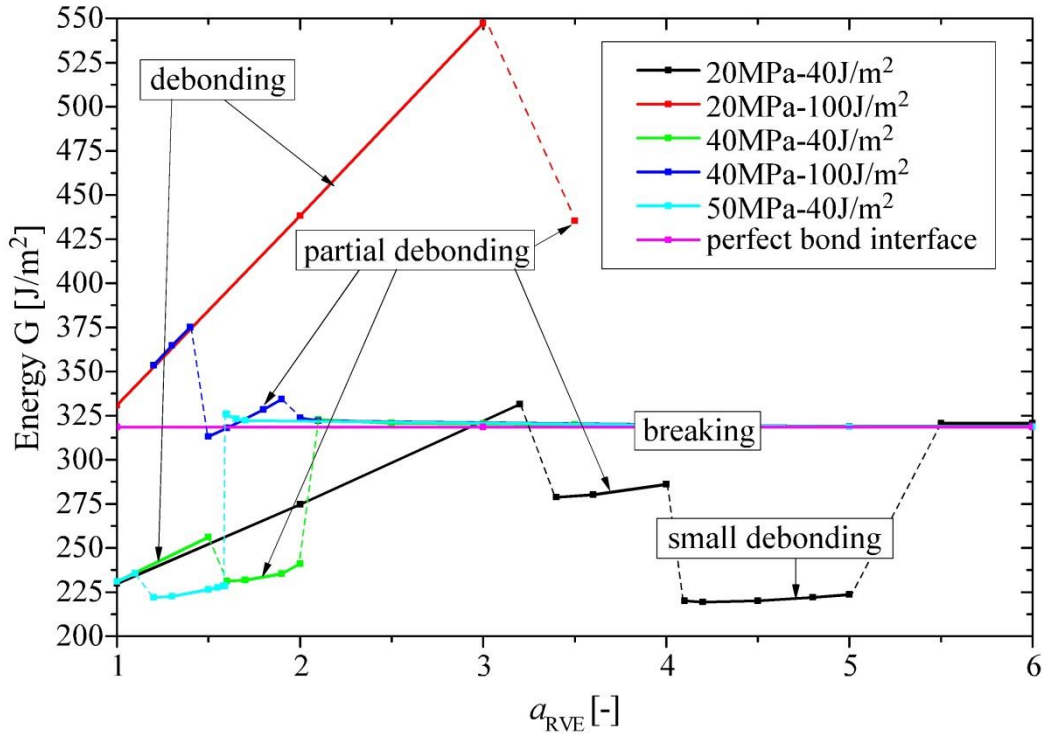


Figure 10: Effect of the ceramic-polymer interfaces on the peak stress and the failure mechanisms for an RVE with  $W = 10 \mu\text{m}$ . Sensitivity of the RVE's fracture energy depending on the cohesive strength and fracture energy of the ceramic-polymer interfaces

#### 4.3. Effect of pre-crack

As already shown in [8, 28], the type of imperfection considered in the fibres has an influence on the resulting macroscopic response of the RVE. In order to analyse this effect, a sensitivity study is given here. Again, an RVE with  $W = 10 \mu\text{m}$  is considered for that purpose. The results are summarised in Figure 11. According to Figure 9, (pure) debonding is observed for small aspect ratios. In this case, the mechanical response of the RVE is obviously independent of the type of imperfection. For this reason, both models (with and without a pre-existing crack) predict the same response (aspect ratio varies between 1.0-1.5). Only if the failure mode changes and crack propagation is involved, both models lead to a different mechanical response. In this connection, the transition to a different failure mode occurs earlier, if a pre-crack is assumed. As expected, the fracture energy and the peak stress are higher for an initially perfect material. Furthermore, in the case of an initially perfect RVE, the fracture energy increases almost discontinuously, if the failure mode switches from debonding to breaking (aspect ratio of approximately 2.3). A similar strong change can also be seen for the RVE with a pre-crack at an aspect ratio of 2.3. Due to the strong sensitivity at this point, a microstructure close to this aspect ratio should be avoided in practice.

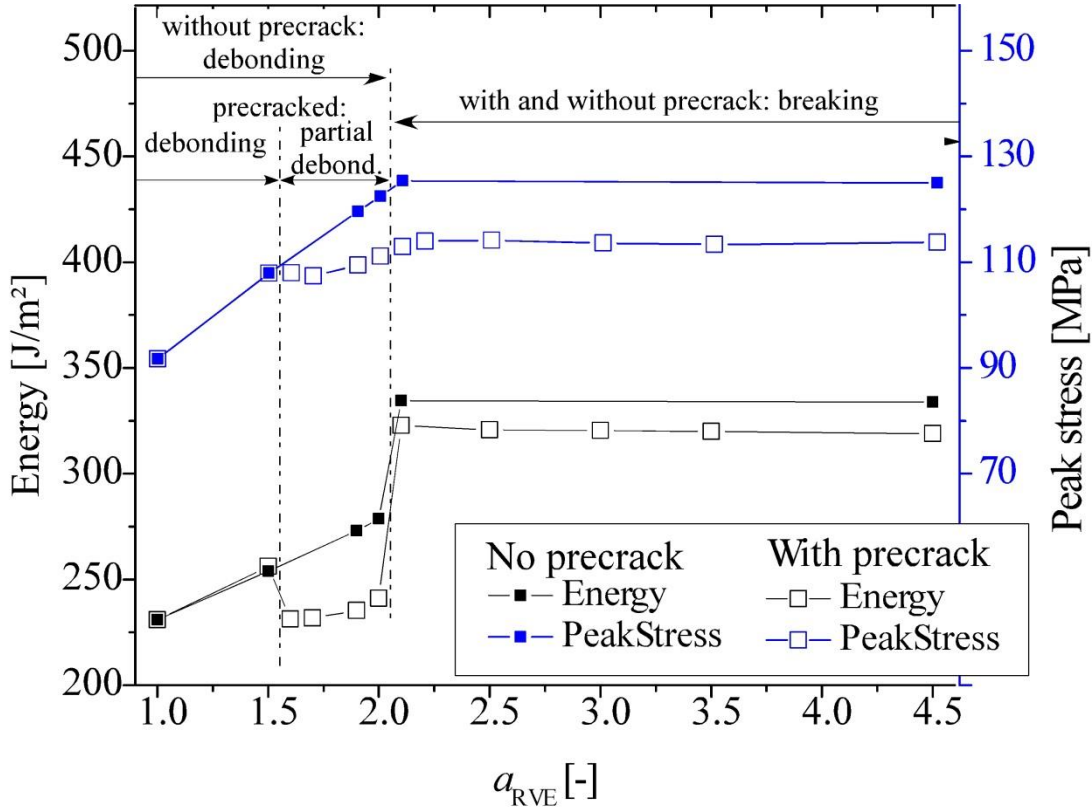


Figure 11: Sensitivity of the RVE's peak stress and fracture energy depending on the initial imperfection (pre-existing crack)

#### 4.4. Comparison with analytical methods

By applying the widely-used shear-lag model, developed initially by Cox [29], one can estimate the limit between the different failure modes fibre breaking and debonding. According to [30], the shear-lag model leads to the following equation for the critical fibre length:

$$l_c = \frac{T_{0,cer}^n R_{fib}}{T_{0,deb}^t} \quad (4)$$

Consequently, this limit depends on the tangential debonding strength and on the fibre strength, but yields a constant critical aspect ratio  $a_{c,fb} = l_c / R_{fib}$ . Equation (4) is the simplest version of shear lag model, which has been extended by several authors, see e.g. [31-33]. In the present case, the analytical limit achieved by eq. (4) using the parameters given in Table 2 is  $a_{fib} = 7.5$  ( $\Rightarrow a_{RVE} = 3.9$ ) for an intact fibre.

In the simulations conducted in section 3 the limit where the failure mechanism changes from the debonding fibre to a breaking fibre (i.e. between *partial debonding* and *small debonding*) is rather at an aspect ratio of 2 ... 2.5. This difference is however not surprising, since in eq. (4):

- no precracked fibre has been assumed (the theoretical fibre strength reduces by 20% due to the cross section reduction, leading to a critical aspect ratio of  $a_{RVE} = 3.1$  for the simple model),
- stress transfer across the fibre ends is not accounted for, and

c) further stress increase upon partial debonding is not included.

A so-called partially elastic model for fibre debonding, [33], avoids all of these shortcomings but with the drawback that no closed-form strain independent solution can be given. In general, the analytical solution for a more accurate model gives smaller values than the one given by eq. (4), which is in accordance with the results shown in Figure 6.

## 5. Conclusion

In the present paper, the fracture properties of fibre-reinforced PMMA have been numerically analysed by means of finite element computations. For that purpose, representative volume elements have been considered in which the mechanical response of PMMA was modeled by a standard rate-independent J2 plasticity model, while material interfaces (cracks or the interfaces between the fibres and the surrounding matrix) were captured by cohesive zone models. Since the energies of such models scale with volume (for the bulk materials) and with surface area (for material interfaces), a size effect is naturally included. Based on this size effect, a sensitivity study of the fracture strength and fracture energy of the composite was performed. It was shown that the diameter and the length of the fibres lead to two different interacting length scales. Depending on such size effects, different types of failure modes have been observed: (a) Pure debonding of the fibres only occurs for small aspect ratios. (b) Small debonding requires low bond strength of the interface between the fibres and the PMMA. This failure mode was only observed for rather large absolute sizes of the RVEs. (c) Partial debonding can only occur if pre-cracks are assumed. (d) Pure breaking. With respect to the design of new composites showing superior fracture properties (high fracture strength and high fracture energy), the composite should fail by pure breaking. In line with the previous work [8, 28], this failure mode can be activated by fibres having a sufficiently small diameter. However, the current sensitivity analysis provides further information: If the fibres are sufficiently thin and simultaneously sufficiently long (small value  $W_{RVE}$  and large value  $a_{RVE}$ ; see Figure 6 and Figure 7), the resulting RVE shows a high fracture strength and high fracture energy – frequently considered as two incompatible properties.

The numerical results also show that the transition between different failure modes does not only depend on the aspect ratio as would be predicted by analytical models like the shear-lag model, but also unveil that the failure mechanism depends on the absolute size of the fibres. This incorporation of an intrinsic size effect is one of the advantages of the cohesive model.

The high fracture strength and the high fracture energy predicted for the small RVEs certainly do not imply the same properties at the macroscale. In biological materials, the superior properties at the lowest scale are conserved at the macroscale through a hierarchical microstructure. In terms of the presented model, one would therefore have two characteristic lengths per scale (length and diameter of the fibres at every of the  $n$  microstructural levels); i.e.,  $2n$  geometrical parameters in total. One might expect that optimising these parameters can lead to new materials with outstanding properties.

## Acknowledgements

Financial support from the Hamburg Ministry of Science and Research and the Joachim Hertz Stiftung as part of the Hamburg Initiative for Excellence in Research (LEXI) as well as from the German Research Foundation (DFG) via SFB 986 (M<sup>3</sup>), project A5, is gratefully acknowledged.

## References

1. Bechtle, S., S.F. Ang, and G.A. Schneider, *On the mechanical properties of hierarchically structured biological materials*. Biomaterials, 2010. **31**(25): p. 6378-6385.
2. Meyers, M.A., et al., *Structural Biological Composites: An Overview*. Journal of Materials, 2006. **58**(7): p. 35-41.
3. Espinosa, H.D., et al., *Merger of structure and material in nacre and bone - Perspectives on de novo biomimetic materials*. Progress in Materials Science, 2009. **54**(8): p. 1059-1100.
4. Gao, H. and S. Chen, *Flaw Tolerance in a Thin Strip Under Tension*. Journal of Applied Mechanics, 2005. **72**: p. 732-337.
5. Gao, H., *Application of fracture mechanics concepts to hierarchical biomechanics of bone and bone-like materials*. Int. J. Fract., 2006. **138**: p. 101-137.
6. Kanzaki, S., et al., *Recent progress in the synergy ceramics project*. Key Engineering Materials, 1999. **161-163**: p. 437-442.
7. Pugno, N.M. and A. Carpinteri, *Design of micro-nanoscale bio-inspired hierarchical materials*. Philos. Mag. Letters, 2008. **88**(6): p. 397-405.
8. Scheider, I., et al., *Size effects in short fibre reinforced composites*. Engineering Fracture Mechanics, 2012: p. 1-11.
9. Brandt, K., et al., *Novel ceramic-polymer composites synthesized by compaction of polymer-encapsulated TiO<sub>2</sub>-nanoparticles*. Composites Science and Technology, 2011. **72**: p. 65-71.
10. Mishnaevsky Jr., L., *Computational Mesomechanics of Composites*. 2007, Chichester: Wiley.
11. Gitman, I.M., H. Askes, and L.J. Sluys, *Representative volume: Existence and size determination*. Engineering Fracture Mechanics, 2007. **74**(16): p. 2518-2534.
12. Nguyen, V.P., et al., *Computational homogenization for multiscale crack modeling. Implementational and computational aspects*. International Journal for Numerical Methods in Engineering, 2010. **89**: p. 192-226.
13. Cao, Y., X. Qian, and N. Huber, *Spherical indentation into elastoplastic materials: Indentation-response based definitions of the representative strain*. Materials Science and Engineering: A, 2007. **454-455**(0): p. 1-13.
14. Mark, J.E., *Polymer Data Handbook*. 1999, Oxford: Oxford University Press Inc.
15. Larsson, P.L. and S. Carlsson, *On microindentation of viscoelastic polymers*. Polymer Testing, 1998. **17**(1): p. 49-75.
16. Tvergaard, V., *Effect of fibre debonding in a whisker-reinforced metal*. Mater. Sci. Eng., 1990. **A125**: p. 203-213.
17. Ghosh, S., et al., *Interfacial debonding analysis in multiple fiber reinforced composites*. Mechanics of Materials, 2000. **32**(10): p. 561-591.
18. Scheider, I., *Micromechanical based derivation of traction-separation laws for cohesive model simulations*. Procedia Engineering, 2009. **1**: p. 17-21.
19. Chandra, N., et al., *Some issues in the application of cohesive zone models for metal-ceramic interface*. Int. J. Solids Struct., 2002. **39**: p. 2827-2855.
20. Kraft, R.H., et al., *Computational micromechanics of dynamic compressive loading of a brittle polycrystalline material using a distribution of grain boundary properties*. Journal of the Mechanics and Physics of Solids, 2008. **56**: p. 2618-2641.
21. Luther, T. and C. Könke, *Polycrystal models for the analysis of intergranular crack growth in metallic materials*. Engineering Fracture Mechanics, 2009. **76**: p. 2332-2343.

22. Zavattieri, P.D., P.V. Raghuram, and H.D. Espinosa, *A computational model of ceramic microstructures subjected to multi-axial dynamic loading*. J. Mech. Phys. Solids, 2001. **49**: p. 27-68.
23. Mosler, J. and I. Scheider, *A thermodynamically and variationally consistent class of damage-type cohesive models*. Journal of the Mechanics and Physics of Solids, 2011. **59**(8): p. 1647-1668.
24. Ltd., T.T. *Polymer Data File: Polymethyl Methacrylate - PMMA*. 2010; Available from: <http://www.tangram.co.uk/TI-Polymer-PMMA.html>.
25. Murphy, N. and A. Ivankovic, *The prediction of dynamic fracture evolution in PMMA using a cohesive zone model*. Eng. Fract. Mech., 2005. **72**: p. 861-875.
26. AZoM.com. *Titanium Dioxide - Titania ( TiO<sub>2</sub>)*. 2002; Available from: <http://www.azom.com/article.aspx?ArticleID=1179>.
27. Kishi, Y., et al., *High strength, electrically conductive pore-free TiO<sub>2</sub> ceramics made by hot isostatic pressing*. Journal of Materials Research, 1997. **12**(4): p. 1056-1061.
28. Scheider, I., et al., *Size Effect in the Damage Behaviour of Short Fibre Reinforced Composites*, in *Crack Path, 2012*, A. Carpinteri, et al., Editors. 2012: Gaeta, Italy. p. 1-8.
29. Cox, H.L., *The elasticity and strength of paper and other fibrous materials*. British Journal of Applied Physics, 1952. **3**: p. 73-79.
30. Kelly, A. and W.R. Tyson, *Tensile properties of fibre-reinforced metals: copper/tungsten and copper/molybdenum*. Journal of the Mechanics and Physics of Solids, 1965. **13**(6): p. 329-338.
31. Kim, H., *Effects of fiber aspect ratio evaluated by elastic analysis in discontinuous composites*. Journal of Mechanical Science and Technology, 2008. **22**(3): p. 411-419.
32. Hsueh, C.-H., *A modified analysis for stress transfer in fibre-reinforced composites with bonded fibre ends*. Journal of Materials Science, 1995. **30**: p. 219-224.
33. Lacroix, T., et al., *Modelling of critical fibre length and interfacial debonding in the fragmentation testing of polymer composites*. Composites Science and Technology, 1992. **43**: p. 379-387.